Polarization-Dependent Optical Nonlinearities of Multiquantum-Well Laser Amplifiers Studied by Four-Wave Mixing

Roberto Paiella, *Student Member, IEEE,* Guido Hunziker, Uzi Koren, and Kerry J. Vahala, *Member, IEEE*

***Abstract*— We present a detailed study of the polarization properties of four-wave mixing in multiquantum-well (MQW) semiconductor optical amplifiers (SOA's). In particular, the polarization selection rules relevant to all processes contributing to the generation of the four-wave mixing signal are rigorously derived and discussed. We then show the importance of these results in applications where four-wave mixing is used as a spectroscopic tool to study the optical nonlinearities of semiconductor gain media. For illustration, we demonstrate two novel applications of polarization-resolved four-wave mixing. The first is a new technique for measuring the recombination lifetime in SOA's, based on mixing of a pump wave with polarized amplified spontaneous emission noise. In the second, we use the same polarization selection rules to measure the interwell transport lifetime in alternating-strain MQW amplifiers. Finally, we also discuss the possibility of studying the dynamics of the optically induced phase coherence between spin-degenerate states.**

I. Introduction

SEMICONDUCTOR lasers and semiconductor optical amplifiers (SOA's) are characterized by large ultrafast optical nonlinearities [1]–[7] that strongly affect their dynamic and spectral properties. For instance, the large nonlinear gain compression typical of diode lasers is directly related to the maximum modulation bandwidth achievable in these devices [8]. Furthermore, the same saturation processes are responsible for cross-talk among different optical channels and for the distortion and chirping of short pulses [9] in SOA's. These features obviously pose serious limitations to the use of these amplifiers as in-line repeaters in optical communication networks, for which gain linearity is highly desirable. On the other hand, the nonlinear interaction among different channels in SOA's makes them promising candidates for applications involving wavelength conversion [10] and, in general, all-optical signal processing.

In general, three mechanisms contribute to the strong dependence of both the gain and the refractive index of a semiconductor on the optical field intensity; namely: carrier depletion, carrier heating and spectral hole burning. Carrier depletion refers to the reduction of the overall carrier density, and hence, of the optical gain, brought about by stimulated electron-hole recombination, and as such takes place on a characteristic time scale on the order of the recombination lifetime τ_s, typically a few hundreds of picoseconds. Stimulated recombination, as well as free-carrier and two-photon absorption, also heats the carrier distributions above the lattice temperature, which leads to a further compression of the gain [3], [4]. The lifetime associated with this mechanism is the carrier–LO phonon scattering time, which has been measured to be approximately 650 fs [5], [11]. With both of these mechanisms, the nonlinear gain reduction is accompanied by a large change in the refractive index. Spectral hole burning refers to the reduction of the occupation probabilities of the electronic states (hence once again of the gain coefficient) resonantly interacting with the optical field [1], [2]. This reduction persists on a time scale set by carrier–carrier scattering (typically on the order of 100 fs). In addition to the above interband and intraband nonlinearities, multiquantum-well (MQW) active regions are characterized by an additional, structure-dependent source of optical nonlinearity. This is related to interwell carrier transport and phonon-mediated capture/escape processes between QW states and the overlaying continuum of unconfined states [12]–[18]. The relevance of this mechanism to the maximum modulation bandwidth of quantum-well (QW) lasers is now well established.

In recent years, nondegenerate four-wave mixing (FWM) in SOA's [11], [19]–[22] has emerged as a useful frequency-domain technique for the direct observation of these nonlinearities. In these experiments, two input waves at different frequencies, the pump and the probe, are coupled into the semiconductor active layer, so that the overall optical intensity includes a harmonic component at their difference frequency. The gain and refractive index are then modulated at this frequency by way of all of the mechanisms just discussed. The resulting dynamic gain and index gratings partially scatter the input waves into new sideband signals, whose relative intensities are measured as a function of the pump-probe detuning frequency. The ultrashort relaxation lifetimes governing intraband dynamics can then be accurately determined, since they are mapped to a wide frequency span. Furthermore, because of the large magnitude and ultrafast nature of the nonlinearities involved, FWM in SOA's is also a promising candidate for the implementation of broadband wavelength conversion in wavelength division multiplexed communication networks [23], [24].

Manuscript received January 22, 1997; revised April 2, 1997. This work was supported by the Advanced Research Projects Agency under Contract DAAL 01-94-K-03430 and by the National Science Foundation under Grant ECS-9412862.

R. Paiella, G. Hunziker, and K. J. Vahala are with the Department of Applied Physics, California Institute of Technology, Pasadena, CA 91125 USA.

U. Koren is with Bell Laboratories, Lucent Technologies, Holmdel, NJ 07733 USA.

Publisher Item Identifier S 1077-260X(97)05124-1.

The efficiency of any nonlinear optical process such as FWM strongly depends on the polarization states of the optical waves involved. This issue is particularly important in (multi)QW gain media due to the large anisotropy in their optical response, which immediately follows from the presence of a preferred direction in the active region, the growth axis. In this paper, we present a detailed study of the polarization properties of the optical nonlinearities of such gain media, as embodied in the FWM susceptibility tensor [25]. The importance of this study is twofold. On the one hand, in applications such as wavelength conversion, it is of paramount importance to minimize the dependence of the conversion efficiency on the polarization of the input signal. This issue has been considered elsewhere [25], [26]. Secondly, as is shown in the bulk of this paper, the same polarization properties can be exploited to extend the scope of FWM as a spectroscopic tool.

In the first part of the paper (Section II) the FWM susceptibility tensor is rigorously derived. The simplest theoretical description of FWM processes in SOA's [19], [21] treats the semiconductor gain medium as a collection of inhomogeneously broadened, independent two-state systems (each corresponding to a different point in $\vec{k}$ space). While this approach has been successfully used to account for the dependence of the FWM conversion efficiency on the pump-probe detuning frequency, it is inadequate to describe polarization effects. In order to include such effects, we consider here a multi-state model for the case of (multi)QW SOA's, including the spin-degenerate states in the lowest conduction and valence subbands at a same $\vec{k}$. The results of this analysis are given a simple interpretation in terms of photon transition diagrams, and the FWM polarization selection rules are then derived and discussed.

Section III is devoted to several applications of these results. In particular, in Section III-A, we first present and demonstrate a simple method of measuring the recombination lifetime, based on FWM of a single-frequency pump wave with properly polarized amplified spontaneous emission noise. Next, in Section III-B, polarization-resolved FWM is used to study interwell carrier dynamics in a SOA consisting of alternating pairs of tensile and compressively strained QW's. The model of Section II is extended to account for interwell coupling, which then allows us to infer from the experimental data an estimate for the interwell transport lifetime. Finally, in Section III-C, we discuss the possibility of obtaining FWM with a TE-polarized pump and a TM-polarized probe (or vice versa), in which case the dynamic gratings arise from modulation of the optically induced phase coherence between spin-degenerate states. However, we find that in the device used in our experiments this contribution is exceedingly small due to large birefringence.

II. General Theory

A. FWM Susceptibility Tensor

In the following analysis, we consider the usual case of a pump wave $\vec{E}^{(p)}$ of frequency ω_p and a probe wave $\vec{E}^{(q)}$ of frequency ω_q traveling along the plane of the QW. The pump is assumed to be significantly stronger than the probe so that only the FWM signal at frequency $\omega_s = 2\omega_p - \omega_q$ need be considered. The FWM susceptibility tensor χ_{ijkl} is defined so that the harmonic component of the induced polarization density at ω_s is $P_i^{(s)} = \chi_{ijkl} E_j^{(p)} E_k^{(p)} (E_l^{(q)})^*$, where the indexes j and k refer to the pump components involved in the scattering process and the modulation process, respectively. We calculate this tensor from the microscopic expression for $\vec{P}$,

$$\vec{P}(t) = \frac{1}{V} \sum_{\vec{k},v,c} \rho_{cv}(t) \vec{\mu}_{cv}^{*}. \tag{1}$$

where the index $c(v)$ runs over the two spin-degenerate states in the conduction (valence) subband (only one conduction and one valence subbands are considered). Strict conservation of the two-dimensional (2-D) crystal wavevector $\vec{k}$ in optical transitions is assumed. Furthermore, $\vec{\mu}$ is the electric dipole moment operator, and ρ the density matrix of the electronic system. Note that here and in the following, the explicit dependence on $\vec{k}$ is omitted for notational simplicity.

The time evolution of the polarization function ρ_{cv} is coupled by the optical field to that of the occupation probabilities ρ_{xx} $(x = c, v)$ and of the coherence functions $\rho_{xx'}$ (with $x \neq x'$) according to the usual two-band Bloch equations [27]

$$\dot{\rho}_{cv} + \left(i\omega_{cv} + \frac{1}{\tau_{cv}} \right) \rho_{cv} = \frac{i}{\hbar} \left(\sum_{v'} \vec{\mu}_{cv'} \rho_{v'v} - \sum_{c'} \rho_{cc'} \vec{\mu}_{c'v} \right) \cdot \vec{E}(t) \tag{2}$$

$$\dot{\rho}_{v'v} + \frac{1}{\tau_{v'v}} (\rho_{v'v} - f_v \delta_{v',v}) = \frac{i}{\hbar} \sum_{c'} (\vec{\mu}_{c'v'}^{*} \rho_{c'v} - \rho_{c'v'}^{*} \vec{\mu}_{c'v}) \cdot \vec{E}(t) \tag{3}$$

$$\dot{\rho}_{cc'} + \frac{1}{\tau_{cc'}} (\rho_{cc'} - f_c \delta_{c,c'}) = -\frac{i}{\hbar} \sum_{v'} (\rho_{cv'} \vec{\mu}_{c'v'}^{*} - \vec{\mu}_{cv'} \rho_{c'v'}^{*}) \cdot \vec{E}(t) \tag{4}$$

where $\hbar\omega_{cv} = \epsilon_c - \epsilon_v$ is the transition energy, and several phenomenological time constants have been included to account for damping processes. In particular, τ_{cv} is the usual dipole dephasing lifetime, and $1/\tau_{xx'}$ is the rate at which $\rho_{xx'}$ relaxes to its quasiequilibrium value (i.e., the quasi-Fermi distribution f_x for $x = x'$, zero otherwise), due to carrier–carrier scattering. In the following, we will take for simplicity $\tau_{xx} = \tau_1$ for all x and $\tau_{xx'} = \tau_2$ for $x \neq x'$. Notice that forward and exchange scattering processes (i.e., carrier–carrier interactions leaving the overall distribution unchanged) contribute to τ_2 but not to τ_1, so the latter is expected to be somewhat longer.

Since f_x is a function of the carrier density N and subband temperature T_x, we obtain a closed set of equations by

including the rate equations [21]

$$\dot{N}+\frac{N}{\tau_s}=-\frac{i}{\hbar}\frac{1}{V}\sum_{\vec{k},v,c}(\rho_{cv}\vec{\mu}^{*}_{cv}-\vec{\mu}_{cv}\rho^{*}_{cv})\cdot\vec{E}(t) \quad (5)$$

$$\dot{T}_x+\frac{T_x-T_L}{\tau_h^x}=-\frac{i}{\hbar}\frac{1}{V}\sum_{\vec{k},v,c}\frac{\epsilon_x-\mu_x}{h_x}\times(\rho_{cv}\vec{\mu}^{*}_{cv}-\vec{\mu}_{cv}\rho^{*}_{cv})\cdot\vec{E}(t) \quad (6)$$

where τ_s and τ_h^x are the interband recombination and carrier–phonon relaxation lifetimes respectively, T_L is the lattice temperature, and μ_x and h_x are the chemical potential and heat capacity of subband $x=c',v'$. Notice that these equations assume an active region consisting of perfectly uncoupled QW's. The inclusion of interwell transport leads to additional contributions to χ_{ijkl} and is considered in Section III-B. Finally, we point out that intraband absorption via plasma heating and two-photon absorption, which may also give a nonnegligible contribution to the FWM susceptibility, are not considered here.

In the presence of two excitation frequencies, ω_p and ω_q, dynamic gratings in the gain and refractive index are formed through carrier density modulation (CDM), carrier heating (CH), and spectral hole burning (SHB). These mechanisms arise respectively from the dependence of the carrier density N, the carrier temperatures T_x, and the occupancy distribution and coherence functions $\rho_{xx'}$ on the optical field intensity, which involves a beat note at the pump-probe detuning frequency $\Omega=\omega_p-\omega_q=\omega_s-\omega_p$. Subsequent scattering of the pump from these gratings produces a harmonic component of the polarization function ρ_{cv} at the converted signal frequency ω_s. Based on these arguments, we assume solutions of the form

$$\begin{aligned}N&=N^{(0)}+(N^{(\Omega)}e^{-i\Omega t}+\text{c.c.})\\ T_x&=T_x^{(0)}+\left(T_x^{(\Omega)}e^{-i\Omega t}+\text{c.c.}\right)\\ \rho_{xx'}&=\rho_{xx'}^{(0)}+\rho_{xx'}^{(\Omega)}e^{-i\Omega t}+\rho_{xx'}^{(-\Omega)}e^{i\Omega t}\\ \rho_{cv}&=\rho_{cv}^{(\omega_p)}e^{-i\omega_p t}+\rho_{cv}^{(\omega_q)}e^{-i\omega_q t}+\rho_{cv}^{(\omega_s)}e^{-i\omega_s t}.\end{aligned} \quad (7)$$

In order to calculate $\rho_{cv}^{(\omega_s)}$, and hence (through (1) and the definition of χ_{ijkl}) the FWM susceptibility tensor, we substitute (7) in the equations of motion (2)–(6), approximate the dependence of f_x on N and T_x with a Taylor series about quasiequilibrium, and retain only terms up to third-order in the input field amplitudes. After some lengthy but straightforward algebra, we find the expression for χ_{ijkl} given in Appendix A, (16)–(19), having general validity within the above framework and for isotropic in-plane dispersion relations. A more compact expression is obtained by neglecting any dependence of $\vec{\mu}_{cv}$ on $|\vec{k}|$, which is in particular a valid approximation in the absence of significant valence-band mixing [28] (e.g., in highly strained QW structures, such as the device used in the experiments described here); the FWM susceptibility tensor is then given by

$$\begin{aligned}\chi_{ijkl}=&\left\langle\sum_{v',c'}(\vec{\mu}_{c'v'})_j(\vec{\mu}_{v'c'})_i\right\rangle\left\langle\sum_{v,c}(\vec{\mu}_{cv})_k(\vec{\mu}_{vc})_l\right\rangle\\ &\times(\chi_{\text{CDM}}+\chi_{\text{CH}})\\ &+\left\langle\sum_{v,c,v'}(\vec{\mu}_{cv})_j(\vec{\mu}_{vc})_i(\vec{\mu}_{cv'})_k(\vec{\mu}_{v'c})_l\right.\\ &\quad\left.+\sum_{v,c,c'}(\vec{\mu}_{vc})_i(\vec{\mu}_{cv})_j(\vec{\mu}_{vc'})_l(\vec{\mu}_{c'v})_k\right\rangle\chi_{\text{SHB}(1)}\\ &+\left\langle\sum_{v,c,v'}(\vec{\mu}_{\bar{c}v})_j(\vec{\mu}_{vc})_i(\vec{\mu}_{cv'})_k(\vec{\mu}_{v'\bar{c}})_l\right.\\ &\quad\left.+\sum_{v,c,c'}(\vec{\mu}_{vc})_i(\vec{\mu}_{c\bar{v}})_j(\vec{\mu}_{\bar{v}c'})_l(\vec{\mu}_{c'v})_k\right\rangle\chi_{\text{SHB}(2)}.\end{aligned} \quad (8)$$

Here, $(\vec{\mu}_{vc})_i$ is the ith component of $\vec{\mu}_{vc}$ ($i=1,2$ for TE and TM components), $\langle\cdots\rangle$ denotes averaging over all directions of $\vec{k}$ on the plane of the QW, and χ_{CDM}, χ_{CH}, $\chi_{\text{SHB}(1)}$, and $\chi_{\text{SHB}(2)}$ are scalar susceptibilities whose explicit expressions are not essential here and are obtained from (16)–(19) as discussed in Appendix A. Furthermore, in the last term on the right-hand side (the term proportional to $\chi_{\text{SHB}(2)}$), the index $\bar{c}$ is defined so that, given c, $\bar{c}\neq c$ (for instance, if c denotes spin-up, $\bar{c}$ denotes spin-down), and similarly for $\bar{v}$.[1]

B. FWM Polarization Selection Rules

The polarization dependence of the FWM susceptibility is entirely contained in the summations over the indices c,v in (16)–(19) [or (8)], where the dipole moment matrix elements in each product have been written in a time-ordered fashion. Notice the different structure in these summations for the cases of carrier density modulation and carrier heating on the one hand, and spectral hole burning on the other. As shown below, this difference is easily explained in terms of the different nature of these mechanisms.

In the case of CDM and CH, the formation of the dynamic gratings (through beating of $E_k^{(p)}$ and $E_l^{(q)}$) and the generation of the converted signal $E_i^{(s)}$ (through scattering of $E_j^{(p)}$ from these gratings) are two entirely distinct processes, hence the two separate summations. In particular, as illustrated schematically in Fig. 1 (left diagram), grating formation involves individual two-photon processes in which a photon is absorbed from the pump and simultaneously emitted into the probe wave. Provided that the final state of the electronic system in each such process is the same as the initial one ($\bar{c}$ in the figure), its occupation probability is correspondingly modulated at the detuning frequency, and then so are the overall carrier density and temperature (since they depend on the states' occupancy integrated over the whole subband). Similarly, the pump is scattered by the resulting gratings into the FWM signal through individual two-photon processes (such as the

[1] If one neglects the difference between the relaxation lifetime τ_1 and the dephasing lifetime τ_2 (so that $\chi_{\text{SHB}(1)}=\chi_{\text{SHB}(2)}$), as was explicitly done in [25], (8) can be cast in the form given there.

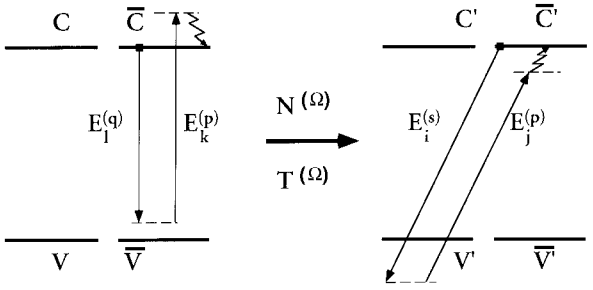

Fig. 1. Photon transition diagrams illustrating the generation of the FWM signal by CDM (CH). Both the modulation of the carrier density (temperatures) and the scattering of the pump into the FWM signal occur through individual two-photon processes, as shown on the left and right diagrams respectively. It is important to point out that the electronic transitions involved in these two steps need not be the same.

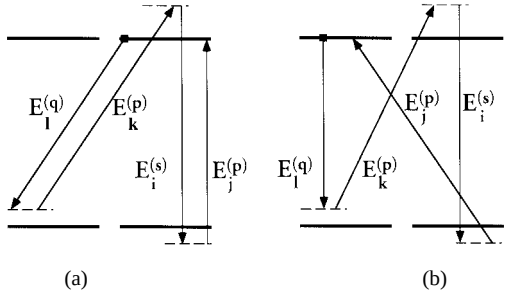

Fig. 2. Photon transition diagrams illustrating the generation of the FWM signal by SHB. In the process shown in (a), the "dynamic gratings" result from modulation of the occupation probability of the initial state of the electronic system. In the process shown in (b), they result from modulation of the optically induced phase coherence between the initial and the second intermediate state. Opposite polarization selection rules apply to these two types of processes.

one shown in the right diagram of Fig. 1), each of which also involves a single electronic transition (between $\bar{c}'$ and v' in the figure). It is important to emphasize that the pump-scattering transitions need not be the same as those involved in the grating formation. Indeed, the states $(c, \bar{c}, v, \bar{v})$ on the one hand and $(c', \bar{c}', v', \bar{v}')$ on the other, as given in Fig. 1, may even be localized in different spatial regions of the active medium. For this reason, FWM by CDM and CH is particularly suited to study the effect of transport processes on the nonlinear optical properties of the given device.

In the case of SHB, however, gain/index modulation and pump scattering occur simultaneously through individual four-photon transitions (hence the single summation). Two qualitatively distinct types of processes are possible, depending on the intermediate states, as illustrated in the diagrams of Fig. 2. In the case shown in Fig. 2(a), the second intermediate state is the same as the initial state, and the gain and index modulation occurs directly through modulation of its occupancy [i.e., dynamic spectral hole burning, described by the term proportional to $\chi_{\mathrm{SHB}(1)}$ in (8)]. As shown in Fig. 2(b), however, photons at the FWM frequency ω_s can also be generated in four-photon processes in which the second intermediate state is different from the initial one. Such processes [which contribute to the term proportional to $\chi_{\mathrm{SHB}(2)}$ in (8)] can still be described in terms of grating formation and pump scattering, but the gratings in this case result from modulation of the optically induced relative phase coherence between the initial and the second intermediate state. The corner frequency of the corresponding contribution to the FWM efficiency is set by the lifetime of this coherence, which, as discussed in connection with (3) and (4), is the dephasing lifetime τ_2 (and not the relaxation lifetime τ_1 which limits the "ordinary" SHB contribution).

The FWM polarization selection rules can be immediately derived from (16)–(19) [or (8)], given knowledge of the dipole moment matrix elements $\vec{\mu}_{vc}$. These are computed from the standard expressions for the spin-degenerate conduction and valence band states in a QW [28] (given in (21) of Appendix A). Once substituted in the summations of (16)–(19) [or (8)], they result in the expressions listed in Appendix A [(22)–(24)]. As can be seen from there, two qualitatively different sets of selection rules are found to apply for processes relying on modulation of the occupation probabilities and for processes relying on modulation of the phase coherence between distinct states.

The former include CDM, CH, and SHB processes of the type illustrated in Fig. 2(a). All such processes are found to give a nonzero contribution only to tensor components of the form χ_{iikk}. In words, this means that: 1) formation of the dynamic gratings by modulation of the occupation probabilities can only occur through beating of the same components of the pump and probe waves (l and k either both TE or both TM) and 2) the TE (TM) component of the pump can be scattered from these gratings only into a TE-(TM-)polarized FWM signal $(i = j)$.

On the other hand, FWM processes relying on modulation of relative coherences [i.e., SHB processes of the type shown in Fig. 2(b)] exhibit exactly the opposite behavior. The dynamic gratings in this case are induced through beating of orthogonal pump and probe components, and scatter each component of the pump into a signal with orthogonal polarization. Therefore, these processes contribute tensor components of the form χ_{ijij} and χ_{ijji} with $i \neq j$.

Notice that these selection rules can be given a simple explanation for the special case of highly-strained QW's, in which, to a high degree of approximation, the relevant valence-band states have pure light-hole (for tensile strain) or heavy-hole (for compressive strain) character. In this case, it is well known that the optical transition between any pair of conduction-band and valence-band states is only allowed to be either TE- or TM-polarized (never both). The above selection rules then immediately follow by inspection of the diagrams of Figs. 1 and 2. Furthermore, compressive wells have negligible gain for TM waves, so that the FWM polarization selection rules further simplify to $\chi_{ijkl} = \chi_{1111}\delta_{i,1}\delta_{j,1}\delta_{k,1}\delta_{l,1}$, and no processes based on modulation of relative coherences are allowed.

C. Polarization Dependence of the FWM Conversion Efficiency

Based on the results discussed in the previous Subsection, we can write the FWM signal field at the SOA output in terms

of the input fields as follows:

$$E_i^{(s)}(L) = \left(E^{(p)}(0)\right)^2 \left(E^{(q)}(0)\right)^* \cdot \left[\left(p_i \sum_{k=1}^{2} M_{iikk} p_k q_k^*\right) + M_{ilil}|_{l\neq i} p_l p_i q_l^* + M_{illi}|_{l\neq i} p_l^2 q_i^*\right] \tag{9}$$

where p_i and q_i are the ith components of the polarization unit vector of the pump and the probe respectively at the SOA input ($i = 1, 2$ for TE and TM components). Furthermore, we define the "transfer tensor" $M_{ijkl} = \chi_{ijkl} R_{ijkl}$, where the factor R_{ijkl} accounts for wave propagation effects; its expression is derived in Appendix B [(30)].

Equation (9) can in principle be used for detailed numerical verifications of experimental results, provided all the relevant material and operational parameters are known. Here, we simply use it to provide a qualitative explanation of the experimentally observed polarization dependence of the FWM conversion efficiency [25]. This same argument is exploited in the applications discussed in the next section. First, notice that the last two terms in (9) are negligible in the sub-terahertz detuning range (where the contribution from SHB is small compared to those from CDM and CH [11]), since both M_{ilil} and M_{illi} $(i \neq l)$ are proportional to $\chi_{\mathrm{SHB}(2)}$. In fact, we will neglect their contribution in most of the remainder.

With this approximation, the polarization selection rules appropriate to CDM and CH apply, and each component of the FWM signal is generated through scattering of the same component of the pump from two "types" of gain and index gratings, i.e., those formed by beating of the TE components of the input waves ("TE-induced gratings") and those formed by beating of their TM components ("TM-induced gratings"). The degree to which these two contributions to $E_i^{(s)}$ add up depends on the relative phase between the two types of gratings, which, in turn, varies with the angle between the polarizations of the beating waves. In particular, as illustrated in the inset of Fig. 3, if the pump and the probe have parallel polarizations, the two types of gratings are in phase, so that their contributions to $E_i^{(s)}$ add constructively and the FWM conversion efficiency is maximum. Vice versa, if the pump and the probe are orthogonally polarized, the two types of gratings are out of phase and tend to cancel each other. However, since the amplitudes associated with the two contributions (i.e., M_{ii11} and M_{ii22}) are in general unequal (see the Appendixes), this cancellation is incomplete. As a result, unlike the case of a perfectly isotropic gain medium, the FWM conversion efficiency of a QW SOA can be finite even for orthogonally polarized pump and probe waves.

This prediction was experimentally verified by measuring the FWM conversion efficiency for different combinations of the pump and probe polarizations. The SOA used has an active region consisting of three pairs of tensile and compressively strained QW's, and was designed to have a polarization-independent small signal gain [29]. We point out, however, that the above discussion is quite general to any (multi)QW SOA, regardless of strain. The detuning frequency was chosen to be small enough (1.5 nm) so that the difference in the birefringence experienced by the two input waves is small and thus the angle between their polarization states remains essentially constant throughout the interaction length. This ensures that any observed variation in the FWM conversion efficiency with the input polarizations is due to the interference between the different types of gratings just described, as opposed to averaging effects associated with birefringence. A typical set of data is shown in Fig. 3, where we plot FWM signal power as a function of the angle of linear polarization of the probe with a linearly polarized pump at $-45°$. The continuous line is a fit to (9), with the coefficients M_{iikk} used as fitting parameters. These results are qualitatively consistent with the discussion of the previous paragraph; in particular, notice the finite FWM conversion efficiency observed even in the case of orthogonal input polarizations.

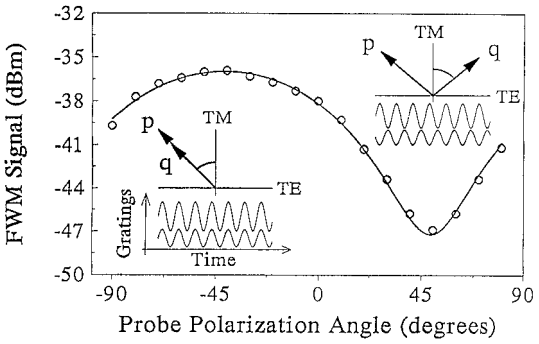

Fig. 3. Converted signal power as a function of the linear polarization angle of the probe relative to the TM direction, with linearly polarized pump at $-45°$, and 1.5-nm detuning. The continuous line is a theoretical fit to (9), with fitting parameters M_{iikk}. The insets show the formation of the dynamic gratings through beating of TE and TM components of pump and probe. The TE-induced gratings and the TM-induced gratings are in phase with each other for parallel input polarizations and out of phase for orthogonal input polarizations.

III. Applications

A. Measurement of the Recombination Lifetime

As a first application of the FWM polarization selection rules, we show in this section how they can be used to determine the stimulated recombination lifetime τ_s in a very straightforward manner [30]. The approach we use here takes advantage of the polarization selection rules by measuring a FWM signal generated along the TE direction from "TM-induced" dynamic gratings. Since the technique requires both TE and TM transitions, the method is not suitable for SOA's with only compressively strained QW's.

The experiment is schematically explained in Fig. 4. Instead of using a laser source as a probe, we use the broad amplified spontaneous emission (ASE) noise from an erbium doped fiber amplifier, filtered in a 1.6-nm optical bandpass filter and centered about the pump laser frequency. We refer to the ASE as the probe, despite the fact that it is not a single-frequency source but rather an incoherent superposition of frequencies. The previous discussion remains valid, with an additional sum over all frequencies in the right hand side of (9). The ASE source is polarized along the TM direction and coupled into the SOA, along with a single-frequency pump wave polarized

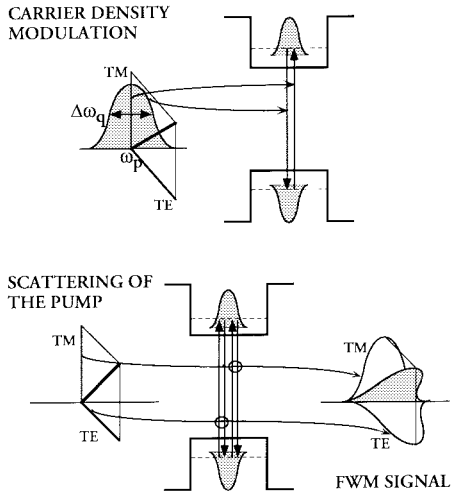

Fig. 4. Schematics of the FWM processes taking place with the polarizations used in the recombination lifetime measurement. In the upper panel, we show the modulation of the carrier density by beating of the input waves (TM components only). In the lower panel, we show the scattering of each pump component into the corresponding FWM component. The probe is not a single frequency source but rather a continuum of frequencies within a 100-GHz bandwidth. The modulation occurs at all these frequencies, and the FWM signal is therefore also a continuum of frequencies.

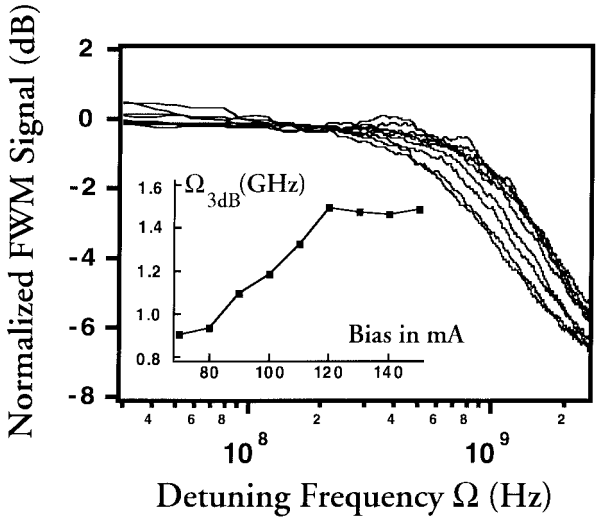

Fig. 5. Results of the recombination lifetime measurement. The TE-polarized FWM efficiency (normalized by the TM polarization emission) is plotted as a function of detuning frequency for SOA bias currents ranging from 50 to 150 mA (left to right). The roll-off associated with the stimulated recombination lifetime is clearly seen; the corresponding 3-dB roll-off frequency $(1/2\pi\tau_s)$ is shown in the inset as a function of the bias current.

at 45° with respect to the growth axis (i.e., equal TE and TM components). The TM components of these input waves will modulate the carrier density at all frequencies within the half-bandwidth of the optical bandpass filter (0–100 GHz). This modulation will result in gain and index modulation for both polarization modes in the SOA, and thus generate a FWM signal along both the TE and the TM directions (from the M_{1122} and M_{2222} terms in (9), respectively).

We select only the TE polarized waves at the output of the SOA by way of a polarization filter. This yields a signal which, upon direct detection, contains the pump-FWM signal beatnote in the RF-frequency domain. On the other hand, since the probe has no component along TE, the pump-probe beatnote (which would otherwise overpower the pump-FWM RF signal) is suppressed with the polarizer. Furthermore, the use of a broad superposition of probe frequencies centered around the pump allows us to map out the detuning frequency dependence of the FWM efficiency (in this case giving the CDM response) in just one scan of the RF-spectrum. The TM components at the SOA output also contain a pump-FWM signal, but the pump-ASE probe beatnote is much stronger at the detector. In fact, we used this latter signal to normalize out the RF-frequency dependence of our detection system.

The results are shown in Fig. 5, where we have plotted the normalized FWM signal versus detuning frequency, measured in an alternating-strain SOA. The corner frequency appears very clearly, from which the stimulated recombination rate can be immediately inferred; its value is shown in the inset for different bias currents to the SOA.

B. Measurement of the Interwell Carrier Transport Lifetime in an Alternating-Strain MQW SOA

As we pointed out in Section II-B, in conjunction with Fig. 1, an important feature of FWM by CDM (and CH) is that the formation of the dynamic gratings and the scattering of the pump into the converted signal are entirely distinct processes. As such, they do not even need to take place in the same spatial region of the SOA. For example, in a MQW SOA with interwell coupling, we may consider a FWM process in which the gratings are formed in one well and then transferred to a neighboring well where the pump is then scattered [31], [32]. The strength of this process strongly depends on the interwell transport rate $1/\tau_t$; in particular, we expect it to become negligibly small at detuning frequencies much larger than this rate. As a result, FWM can be used to measure τ_t, provided that the contribution to the overall FWM signal associated with the above process can somehow be isolated from all other contributions. As we will show in the following, this can be done by taking advantage of the FWM polarization selection rules in an alternating-strain SOA. This technique [32] provides an extremely clean way of studying interwell transport, which is an issue of considerable importance given its relation to the maximum achievable modulation bandwidth of MQW lasers [12], [13], [15]. Notice that the use of polarization selection rules to discriminate between the contribution from tensile and compressive wells in a similar SOA has also been recently employed in pump-probe time-domain measurements [18].

The FWM polarization configuration required in this work is illustrated in Fig. 6: once again, the SOA consists of alternating pairs of tensile and compressive wells; the probe is linearly polarized along the growth axis (TM polarization), whereas both the TE and the TM components of the pump are nonzero (and equal to each other for simplicity). We only consider detuning frequencies below 100 GHz, so that CDM provides the strongest FWM mechanism. Then, as shown in the upper panel of Fig. 6, the beating of the input waves only results in "TM-induced gratings," which can be generated only in the tensile wells. Here, each polarization component of

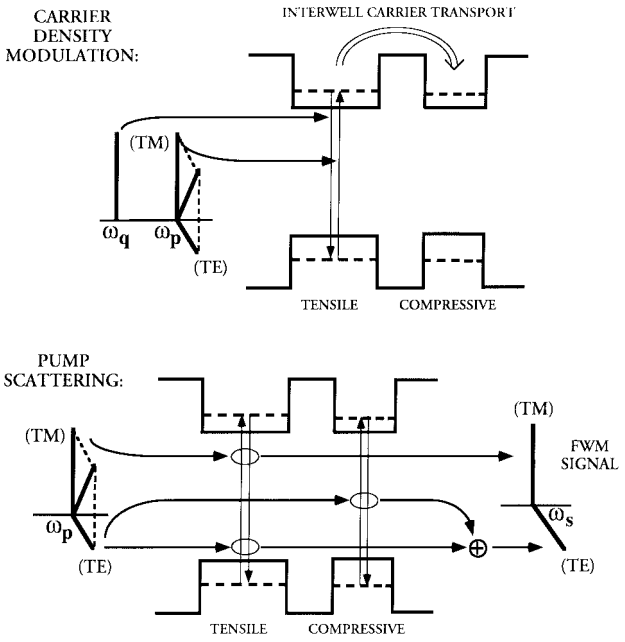

Fig. 6. Schematics of the FWM processes taking place with the polarizations used in the interwell transport lifetime measurement. As shown in the upper panel, modulation of the carrier density is generated directly (through beating of the TM components of the input waves) only in the tensile wells, from which it can then be transferred to the neighboring compressive wells. Each polarization component of the pump is then correspondingly scattered into the same component of the FWM signal as shown in the lower panel.

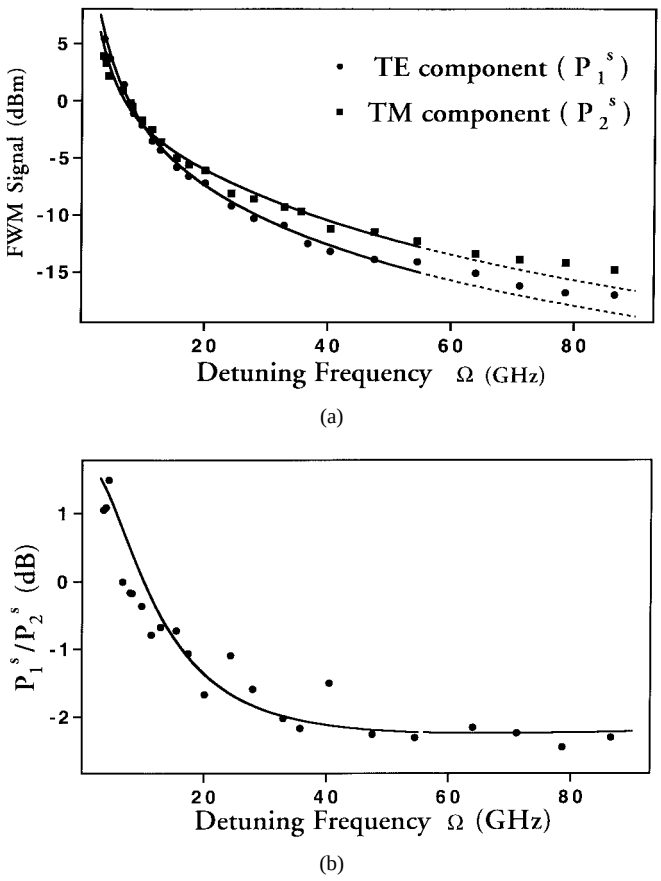

Fig. 7. Results of the interwell transport lifetime measurement. The optical powers in the TE (circles) and TM (squares) components of the FWM signal (a), and their ratio (b) are plotted versus detuning frequency. The continuous lines are fits to the model theory discussed in the text. As emphasized by the dashing, the fit becomes inaccurate in Fig. 7(a) at detuning frequencies above 50 GHz, where carrier heating, not included in the fit, becomes important. However, since its contribution is approximately the same for both the TE and the TM components, the fit remains good for their ratio in Fig. 2(b). An approximate transport lifetime of 16 ps is inferred from the data.

the pump is then scattered into the same component of the FWM signal. Furthermore, if the carrier density modulation underlying the dynamic gratings can be transfered into the neighboring compressive wells, an additional contribution to the TE component of the converted signal can be generated there. The lower panel of Fig. 6 gives a schematic representation of the different processes contributing to the FWM signal field $\vec{E}^{(s)}$, which can accordingly be written as

$$\begin{aligned} E_1^{(s)} &= R_{1122}\left(\chi_{1122}^T + \chi_{1122}^{C\leftarrow T}\right)\left(E^{(p)}\right)^2\left(E^{(q)}\right)^* \\ E_2^{(s)} &= R_{2222}\chi_{2222}^T\left(E^{(p)}\right)^2\left(E^{(q)}\right)^*. \end{aligned} \tag{10}$$

In these expressions, the subscript $i = 1, 2$ denotes the TE and TM directions respectively, and we have taken $\vec{E}^{(q)} = \hat{e}_2 E^{(q)}$ and $\vec{E}^{(p)} = (\hat{e}_1 + \hat{e}_2)E^{(p)}$. Furthermore, the superscripts T and C are used to distinguish between quantities in the tensile and compressive wells, and the term proportional to $\chi_{1122}^{C\leftarrow T}$ describes the contribution involving interwell transport.

With this choice for the polarization states of the input waves, information about the interwell coupling is obtained by plotting P_1^s/P_2^s (P_i^s denoting the optical power in the ith component of the FWM signal) versus detuning frequency. The wave propagation factors R_{iikk} can be regarded as independent of Ω over the small detuning range (<100 GHz) considered in this work (see Appendix B), so that we may regard $P_1^s/P_2^s(\Omega) \propto |(\chi_{1122}^T + \chi_{1122}^{C\leftarrow T})/\chi_{2222}^T|^2$. Consequently, we expect this curve to approach a constant value (proportional to $|\chi_{1122}^T/\chi_{2222}^T|^2$) as Ω exceeds the interwell transport rate. Any feature observed at lower detuning frequencies, on the other hand, can be ascribed to interwell coupling. These expectations are borne out by the data shown in Fig. 7, where we plot the measured optical powers in the TE and TM components of the FWM signal [Fig. 7(a)], and their ratio [Fig. 7(b)]. The experimental setup consisted of a high sensitivity optical heterodyne detection system, and is described elsewhere [11].

The experimental data shown in Fig. 7 can be fitted using the theoretical framework of the previous section, provided this is properly generalized to include a simple model for the interwell carrier dynamics. In particular, we assume that the transfer of carriers between neighboring wells mainly results from phonon-assisted capture/escape processes between 2-D QW states and semiclassical wavepackets of three-dimensional (3-D) states localized near the same well [14], [15]. We describe the dynamics of these wavepackets as dominated by classical diffusion. Drift, on the other hand, is expected to be of minor importance, due to the nearly flat-band conditions typical of forward-bias SOA operation [14], [15]. Tunneling is also neglected, which is a fair assumption given the relatively large barrier width L_b (100 Å) in the SOA under study. Furthermore, the dynamics of holes, which are known to a have a shorter capture lifetime [15], is not considered explicitly.

With these assumptions, the Bloch equations (2)–(4) remain appropriate, except that two distinct sets of such equations are required for the two types of wells. The interwell coupling is then introduced in the model by replacing the rate equation for the carrier density, (5), by the following:

$$\dot{N}^X_{2\text{-D}} + \left(\frac{1}{\tau_s} + \frac{1}{\tau^X_{\text{esc}}}\right) N^X_{2\text{-D}} - \frac{N^X_{3\text{-D}}}{\tau^X_{\text{cap}}} = -\frac{i}{\hbar}\frac{1}{V^X}\sum_{\vec{k},v,c}\left(\rho^X_{cv}\vec{\mu}^{X*}_{cv} - \vec{\mu}^X_{cv}\rho^{X*}_{cv}\right)\cdot\vec{E}(t) \qquad X = T, C \quad (11)$$

$$\dot{N}_b + \frac{N_b}{\tau_s} = D\frac{d^2 N_b}{dz^2}. \quad (12)$$

Here, $N_{2\text{-D}}$ denotes the number density of electrons confined inside the QW under consideration; $N_{3\text{-D}}$ is the density of unconfined electrons localized near the same QW so as to be involved in the capture/escape processes; $N_b(z)$ is the density of unconfined electrons as a function of position z along the growth axis; τ_{esc} and τ_{cap} are the quantum escape and capture lifetimes; D is the diffusion coefficient; and again the superscript $X = T, C$ refers to quantities of tensile and compressive wells. In principle, the rate equations for the carrier temperatures should also be generalized in a similar fashion; however, in the experiment described here the detuning frequency is kept small enough that inclusion of CH effects is not critical. Finally, we point out that when the interwell coupling results from resonant tunneling, this description becomes inappropriate and one has to include the coupling directly in the density matrix equations of motion; this has been done in [33], where it is shown that such coupling introduces a resonance peak in the terahertz FWM response.

The coupled equations (11), (12) can be solved given an appropriate set of boundary conditions satisfied by $N_b(z)$ near each QW. For instance, we may require $N_b(z^T_i \pm L^T_w/2) = N^T_{3\text{-D}}$ and $D\frac{dN_b}{dz}(z^T_i \pm L^T_w/2) = \pm\frac{L^T_w}{2}(\frac{N^T_{3\text{-D}}}{\tau^T_{\text{cap}}} - \frac{N^T_{2\text{-D}}}{\tau^T_{\text{esc}}})$, where z^T_i denotes the position of the center of the ith tensile well, of width L^T_w (and similarly for each compressive well). Notice that these conditions introduce further approximations to the model, since they implicitly assume an infinite chain of pairs of oppositely strained wells, and furthermore neglect any diffusion process occurring over the finite width of the wells. In any case, regardless of the detailed form of the boundary conditions (provided they are linear), the solution of (12) can be used to recast (11) in the following form (in the frequency domain):

$$\left(-i\Omega + \frac{1}{\tau^T_e}\right)N^{T(\Omega)}_{2\text{-D}} - \frac{N^{C(\Omega)}_{2\text{-D}}}{\tau^{T\leftarrow C}_t} = -\frac{i}{\hbar}\frac{1}{VT}\sum_{\vec{k},v,c}\left[\rho^{T(\omega_p)}_{cv}\left(\vec{\mu}^T_{cv}\cdot\vec{E}_q\right)^* - \vec{\mu}^T_{cv}\cdot\vec{E}_p\left(\rho^{T(\omega_q)}_{cv}\right)^*\right]$$

$$\left(-i\Omega + \frac{1}{\tau^C_e}\right)N^{C(\Omega)}_{2\text{-D}} - \frac{N^{T(\Omega)}_{2\text{-D}}}{\tau^{C\leftarrow T}_t} = -\frac{i}{\hbar}\frac{1}{VC}\sum_{\vec{k},v,c}\left[\rho^{C(\omega_p)}_{cv}\left(\vec{\mu}^C_{cv}\cdot\vec{E}_q\right)^* - \vec{\mu}^C_{cv}\cdot\vec{E}_p\left(\rho^{C(\omega_q)}_{cv}\right)^*\right] \quad (13)$$

where $1/\tau^T_e$ is an effective escape rate from each tensile well, and $1/\tau^{T\leftarrow C}_t$ is the overall transport rate from each compressive well to each neighboring tensile well. Simple expressions for these quantities can be obtained if: 1) we use the boundary conditions on N_b mentioned above; 2) we take the diffusion length $L_D = \left|\sqrt{\frac{D\tau_s}{1-i\Omega\tau_s}}\right|$ to be much larger than the barrier width L_b (which is certainly the case at the detuning frequencies of interest here); and 3) we neglect differences between the two types of wells. The result is

$$\frac{1}{\tau_t} = \frac{1}{2\tau_{\text{esc}}}\frac{1}{1 - i\Omega\tau_{\text{cap}}L_b/L_w}, \qquad \frac{1}{\tau_e} = \frac{1}{\tau_s} + \frac{1}{2\tau_{\text{esc}}}\frac{1 - i\Omega 2\tau_{\text{cap}}L_b/L_w}{1 - i\Omega\tau_{\text{cap}}L_b/L_w}. \quad (14)$$

Notice how both rates are complex-valued functions of the detuning frequency Ω (the frequency of the carrier density modulation being coupled between adjacent wells). This dependence results from the Ω dependence of the diffusion length; the complex character implies that a phase shift is introduced in the escape/transport process. At low detuning frequencies, where diffusion is essentially instantaneous, interwell transport is mainly limited by quantum escape, and $\tau_t \approx \tau_e \approx 2\tau_{\text{esc}}$ (the factor of two appears because, if the two types of wells have equal capture lifetime, as assumed in (14), each escaped carrier from a well can be transferred to an adjacent well or recaptured in the same well with equal probability).

Given the rate equations (13) and the density matrix equations (2)–(4) for both types of wells, one can proceed as before to solve for the FWM susceptibility tensor components. The contribution from each compressive well can be written as $\chi_{ijkl}|_C = \chi^C_{ijkl} + \chi^{C\leftarrow T}_{ijkl}$, where (including the CDM terms only, as appropriate to the experiment under consideration)

$$\chi^C_{ijkl} = \left\langle\sum_{v',c'}\left(\vec{\mu}^C_{c'v'}\right)_j\left(\vec{\mu}^C_{v'c'}\right)_i\right\rangle\left\langle\sum_{v,c}\left(\vec{\mu}^C_{cv}\right)_k\left(\vec{\mu}^C_{vc}\right)_l\right\rangle\chi^{C\leftarrow C}_{\text{CDM}}$$

$$\chi^{C\leftarrow T}_{ijkl} = \left\langle\sum_{v',c'}\left(\vec{\mu}^C_{c'v'}\right)_j\left(\vec{\mu}^C_{v'c'}\right)_i\right\rangle\left\langle\sum_{v,c}\left(\vec{\mu}^T_{cv}\right)_k\left(\vec{\mu}^T_{vc}\right)_l\right\rangle\chi^{C\leftarrow T}_{\text{CDM}} \quad (15)$$

(the contribution from each tensile well can be written in exactly the same manner with the superscripts T and C interchanged). Again, we are neglecting here any dependence of $\vec{\mu}_{cv}$ on $|\vec{k}|$, as appropriate to highly strained QW's; full expressions for the scalar susceptibilities just defined are given in Appendix A.

The continuous lines in Fig. 7 are the fits to the model theory just described. The agreement with the experimental data is excellent, except for the points at detuning frequencies in excess of about 50 GHz, where carrier heating (not included in the model) is known [11] to cause an increase in the FWM conversion efficiency. Note, however, that since this increase is approximately the same for both the TE and TM components, the fit remains good for their ratio in Fig. 7(b). From this fit, we obtain an estimate of 16 ps for the low-detuning interwell

transport lifetime τ_t, as well as τ_e.[2] Furthermore, if we assume that τ_t and τ_e are related to the quantum capture/escape lifetimes as given by (14), we find $\tau_{\rm esc} \approx 8$ ps, and $\tau_{\rm cap} \approx 1.5$ ps; we point out however that these estimates further rely on the simplifying assumptions used to derive (14), and they should be interpreted accordingly. Anyway, we note that these values are consistent with previous reports [12]–[18] and with the observed maximum modulation bandwidth of QW lasers.

C. Investigation of the Optically Induced Phase Coherence Between Spin-Degenerate States

In the presence of an external optical field, a relative phase coherence may be established between two spin-degenerate states in, say, the conduction band (even if the dipole moment between them is obviously zero), if the field couples both states to a same state in the valence band. In particular, if the optical intensity involves a beat note at some frequency Ω (as in the case of FWM), this phase coherence (described, in (2)–(4) by the density matrix elements $\rho_{c\bar{c}}$ with $\bar{c} \neq c$) will be modulated at the same frequency. As was discussed in Section II-B, this can only occur if the beating involves a TE-polarized pump and a TM-polarized probe (or vice versa); the TE (TM) component of the pump is then scattered into a TM-(TE-)polarized FWM signal.

This contribution to the converted signal [described by the last two terms on the right-hand side of (9)] can be easily isolated by setting the polarization state of one of the input waves exactly along the TE direction, and that of the other along the TM direction. The observation of a FWM signal under this condition would allow to study the dephasing dynamics of the spin-spin phase coherence just described. In particular, by measuring the corresponding FWM conversion efficiency versus detuning frequency (and appropriately subtracting all propagation effects), one could extrapolate the dephasing lifetime τ_2.

However, this FWM mechanism is strongly limited in the device used in our experiments, due to the high degree of birefringence typical of most strained MQW SOA's. We estimated the refractive index experienced by TM (TE) waves by measuring the frequency spacing between neighboring TM (TE) residual modes of the SOA; the difference $\Delta n = |n_{\rm TM} - n_{\rm TE}|$ was found to be quite large, approximately equal to 3×10^{-2}. As a result, the phase mismatch between the input waves is in this case significant. This leads to a strong reduction in the FWM conversion efficiency, which can be quantified using (30) below for $R_{ill i}(i \neq l)$. For simplicity, we assume that the total optical intensity is uniform along the interaction length (as appropriate to the high-saturation regime of operation), and furthermore we neglect the frequency dependence of the gain coefficient and refractive index (as appropriate to sub-TeraHertz detuning frequencies). Then, the magnitude squared of $R_{ill i}(i \neq l)$ is found to be smaller than that of R_{iikk} by almost 3 orders of magnitude. In other words, the phase matching requirement reduces the conversion efficiency for FWM with TE-polarized pump and TM-polarized probe (or vice versa) by almost 30 dB.

In a preliminary experiment, we found the FWM conversion efficiency under these conditions to be exceedingly small, so that a lock-in amplifier had to be used in conjunction with our standard optical heterodyne system to even see the converted signal. Possible ways of maximizing its strength are currently under investigation.

[2] Again, we neglect any difference between the relevant time constants in the two types of wells, since we believe that any such difference would be too small to be unambiguously inferred from the data of Fig. 7.

IV. Conclusion

We have reported the results of an extensive theoretical and experimental study of the polarization properties of FWM in MQW SOA's. These results, we believe, are useful for a thorough understanding of the microscopic processes responsible for the generation of the FWM signal. Furthermore, we have shown how they can be used in FWM spectroscopy of the SOAs' optical nonlinearities. In particular, we have demonstrated novel techniques for the measurement of the stimulated recombination lifetime and the interwell transport rate of alternating-strain MQW SOA's.

Appendix A
FWM Susceptibility Tensor Components

In this appendix, we give the explicit expression for the FWM susceptibility tensor χ_{ijkl}, as derived within the framework described in Section II-A. The contributions associated with carrier density modulation, carrier heating and spectral hole burning are as follows:

$$\begin{aligned}\chi_{ijkl}|_{\rm CDM} &= -\frac{i}{\hbar^3}\sum_{x=c',v'}\frac{\tau_s}{1-i\Omega\tau_s}\frac{1}{V} \\ &\cdot\left(\sum_{|\vec{k}|}\frac{1}{1-i\Omega\tau_1}|M|^2\left\langle\sum_{v,c}(\vec{\mu}_{cv})_j(\vec{\mu}_{vc})_i\right\rangle\frac{\partial f_x}{\partial N}\hat{\chi}(\omega_s)\right)\frac{1}{V} \\ &\cdot\left(\sum_{|\vec{k}|}|M|^2\left\langle\sum_{v,c}(\vec{\mu}_{cv})_k(\vec{\mu}_{vc})_l\right\rangle\Delta f(\hat{\chi}(\omega_p)-\hat{\chi}^*(\omega_q))\right)\end{aligned} \tag{16}$$

$$\begin{aligned}\chi_{ijkl}|_{\rm CH} &= -\frac{i}{\hbar^3}\sum_{x=c',v'}\frac{\tau_h^x}{1-i\Omega\tau_h^x}\frac{1}{V} \\ &\cdot\left(\sum_{|\vec{k}|}\frac{1}{1-i\Omega\tau_1}|M|^2\left\langle\sum_{v,c}(\vec{\mu}_{cv})_j(\vec{\mu}_{vc})_i\right\rangle\frac{\partial f_x}{\partial T}\hat{\chi}(\omega_s)\right)\frac{1}{V} \\ &\cdot\left(\sum_{|\vec{k}|}|M|^2\left\langle\sum_{v,c}(\vec{\mu}_{cv})_k(\vec{\mu}_{vc})_l\right\rangle\right. \\ &\quad\left.\cdot\,\Delta f(\hat{\chi}(\omega_p)-\hat{\chi}^*(\omega_q))\frac{\epsilon_x-\mu_x}{h_x}\right)\end{aligned} \tag{17}$$

$$\chi_{ijkl}|_{\mathrm{SHB}(1)} = \frac{i}{\hbar^3}\frac{1}{V}\sum_{|\vec{k}|}\frac{\tau_1}{1-i\Omega\tau_1}|M|^4 \times \left\langle \sum_{v,c,v'} (\vec{\mu}_{cv})_j(\vec{\mu}_{vc})_i(\vec{\mu}_{cv'})_k(\vec{\mu}_{v'c})_l + \sum_{v,c,c'} (\vec{\mu}_{vc})_i(\vec{\mu}_{cv})_j(\vec{\mu}_{vc'})_l(\vec{\mu}_{c'v})_k \right\rangle \times \Delta f\hat{\chi}(\omega_s)(\hat{\chi}(\omega_p)-\hat{\chi}^*(\omega_q)) \quad (18)$$

and

$$\chi_{ijkl}|_{\mathrm{SHB}(2)} = \frac{i}{\hbar^3}\frac{1}{V}\sum_{|\vec{k}|}\frac{\tau_2}{1-i\Omega\tau_2}|M|^4 \times \left\langle \sum_{v,c,v'} (\vec{\mu}_{\bar{c}v})_j(\vec{\mu}_{vc})_i(\vec{\mu}_{cv'})_k(\vec{\mu}_{v'\bar{c}})_l + \sum_{v,c,c'} (\vec{\mu}_{vc})_i(\vec{\mu}_{c\bar{v}})_j(\vec{\mu}_{\bar{v}c'})_l(\vec{\mu}_{c'v})_k \right\rangle \times \Delta f\hat{\chi}(\omega_s)(\hat{\chi}(\omega_p)-\hat{\chi}^*(\omega_q)) \quad (19)$$

where we introduced the matrix element $M = \langle S,\uparrow|ex|X,\uparrow\rangle$, the Fermi inversion factor $\Delta f = f_v - f_c$ and the complex lineshape function

$$\hat{\chi}(\omega) = \frac{1}{\omega-\omega_{cv}+i\tau_{cv}^{-1}}. \quad (20)$$

All Fermi distribution functions are to be evaluated under conditions of quasiequilibrium (as determined by the electrical pumping). Also, in (19), the index $\bar{c}$ is defined so that, given c, $\bar{c}\neq c$ (for instance, if c denotes spin-up, $\bar{c}$ denotes spin-down), and similarly for $\bar{v}$. Furthermore, in writing these expressions, we assumed isotropic in-plane dispersion relations, so that the only quantities depending on the direction of the 2-D wavevector $\vec{k}$ are the dipole moments $\vec{\mu}_{vc}$, and $\langle\cdots\rangle$ denotes averaging over all directions of $\vec{k}$. All other quantities appearing in (16)–(20) are defined in Section II-A.

Next, we consider the summations over the indexes c, v, which, once substituted in (16)–(19), entirely determine the polarization properties of the FWM susceptibility. We consider the general case of a QW with arbitrary (or zero) strain, for which the doubly-degenerate conduction- and valence-band states can be written as [28]

$$\begin{aligned} |C1(2)\rangle &= |f_k^e\rangle \otimes |S,\uparrow(\downarrow)\rangle \\ |V1(2)\rangle &= |f_k^{hh}\rangle \otimes \left(v^*\left|\frac{3}{2},\frac{3}{2}\right\rangle \mp v\left|\frac{3}{2},-\frac{3}{2}\right\rangle\right) + |f_k^{lh}\rangle \otimes \left(w^*\left|\frac{3}{2},-\frac{1}{2}\right\rangle \mp w\left|\frac{3}{2},\frac{1}{2}\right\rangle\right) \\ v &= \frac{1}{\sqrt{2}}e^{i\left(\frac{3\pi}{4}-\frac{3\xi}{2}\right)} \quad w = \frac{1}{\sqrt{2}}e^{i\left(-\frac{\pi}{4}+\frac{\xi}{2}\right)} \\ \xi &= \arctan\left(\frac{k_y}{k_x}\right) \end{aligned} \quad (21)$$

where $|f_k^e\rangle, |f_k^{lh}\rangle, |f_k^{hh}\rangle$ are the envelope-function state vectors for electrons, light holes and heavy holes.

With these expressions used to compute the dipole moment matrix elements, we find

$$\left\langle \sum_{v,c}\vec{\mu}_{cv}\vec{\mu}_{vc}\right\rangle = \left(|\langle f_k^e|f_k^{hh}\rangle|^2 + \frac{1}{3}|\langle f_k^e|f_k^{lh}\rangle|^2\right)\hat{x}\hat{x} + \frac{4}{3}|\langle f_k^e|f_k^{lh}\rangle|^2\hat{z}\hat{z} \quad (22)$$

$$\begin{aligned} &\left\langle \sum_{v,c,v'}\vec{\mu}_{vc}\vec{\mu}_{cv}\vec{\mu}_{cv'}\vec{\mu}_{v'c}\right\rangle \\ &= \left\langle \sum_{v,c,c'}\vec{\mu}_{vc}\vec{\mu}_{cv}\vec{\mu}_{c'v}\vec{\mu}_{vc'}\right\rangle \\ &= \left(\frac{1}{2}|\langle f_k^e|f_k^{hh}\rangle|^4 + \frac{2}{3}|\langle f_k^e|f_k^{hh}\rangle|^2|\langle f_k^e|f_k^{lh}\rangle|^2 + \frac{1}{18}|\langle f_k^e|f_k^{lh}\rangle|^4\right)\hat{x}\hat{x}\hat{x}\hat{x} \\ &\quad + \left(\frac{2}{3}|\langle f_k^e|f_k^{hh}\rangle|^2|\langle f_k^e|f_k^{lh}\rangle|^2 + \frac{2}{9}|\langle f_k^e|f_k^{lh}\rangle|^4\right) \times (\hat{x}\hat{x}\hat{z}\hat{z}+\hat{z}\hat{z}\hat{x}\hat{x}) + \frac{8}{9}|\langle f_k^e|f_k^{lh}\rangle|^4\hat{z}\hat{z}\hat{z}\hat{z} \end{aligned} \quad (23)$$

$$\begin{aligned} &\left\langle \sum_{v,c,v'}\vec{\mu}_{vc}\vec{\mu}_{\bar{c}v}\vec{\mu}_{cv'}\vec{\mu}_{v'\bar{c}}\right\rangle \\ &= \left\langle \sum_{v,c,c'}\vec{\mu}_{vc}\vec{\mu}_{c\bar{v}}\vec{\mu}_{c'v}\vec{\mu}_{\bar{v}c'}\right\rangle \\ &= \left(\frac{2}{3}|\langle f_k^e|f_k^{hh}\rangle|^2|\langle f_k^e|f_k^{lh}\rangle|^2 + \frac{2}{9}|\langle f_k^e|f_k^{lh}\rangle|^4\right) \times (\hat{x}\hat{z}\hat{x}\hat{z}+\hat{z}\hat{x}\hat{z}\hat{x}) \\ &\quad - \left(\frac{2}{3}\left(\langle f_k^{hh}|f_k^e\rangle\langle f_k^e|f_k^{lh}\rangle\right)^2 + \frac{2}{9}|\langle f_k^e|f_k^{lh}\rangle|^4\right)\hat{x}\hat{z}\hat{z}\hat{x} \\ &\quad - \left(\frac{2}{3}\left(\langle f_k^{lh}|f_k^e\rangle\langle f_k^e|f_k^{hh}\rangle\right)^2 + \frac{2}{9}|\langle f_k^e|f_k^{lh}\rangle|^4\right)\hat{z}\hat{x}\hat{x}\hat{z} \end{aligned} \quad (24)$$

where we use $\hat{x}$ and $\hat{z}$ to denote the TE and TM direction respectively. From these equations, the FWM polarization selection rules discussed in Section II-B are immediately derived.

A more compact expression for χ_{ijkl} can be obtained from (16)–(19), if the dependence of the dipole moment matrix elements on $|\vec{k}|$ can be neglected, which is in particular a valid approximation when valence-band mixing is negligible [28] (i.e., in highly strained structures). Then, the summations over the indexes c, v can be taken out of the sums over $|\vec{k}|$, which results in the general form for χ_{ijkl} given in (8). The scalar susceptibilities χ_{CDM}, χ_{CH}, $\chi_{\mathrm{SHB}(1)}$, and $\chi_{\mathrm{SHB}(2)}$ introduced there can then be immediately obtained from (16) to (19) respectively [by comparison with (8)]. In passing, we note that the limiting forms of (22)–(24) appropriate to highly tensile-strained (compressively strained) QW's are obtained by taking $|f_k^{hh}\rangle \to 0 (|f_k^{lh}\rangle \to 0)$.

$$\chi_{\rm CDM}^{C\leftarrow C}=-\frac{i}{\hbar^3}\sum_{x=c,v}\frac{\tau_e^C\left(1-i\Omega\tau_e^T\right)}{\left(1-i\Omega\tau_e^C\right)\left(1-i\Omega\tau_e^T\right)-\tau_e^C\tau_e^T/\left(\tau_t^{C\leftarrow T}\tau_t^{T\leftarrow C}\right)}$$
$$\times\frac{1}{V^C}\left(\sum_{|\vec{k}|}\frac{1}{1-i\Omega\tau_1}|M^C|^2\frac{\partial f_x^C}{\partial N}\hat{\chi}^C(\omega_s)\right)\frac{1}{V^C}\left(\sum_{|\vec{k}|}|M^C|^2\Delta f^C(\hat{\chi}^C(\omega_p)-(\hat{\chi}^C(\omega_q))^*)\right) \tag{25}$$

$$\chi_{\rm CDM}^{C\leftarrow T}=-\frac{i}{\hbar^3}\sum_{x=c,v}\frac{\tau_e^C\tau_e^T/\tau_t^{C\leftarrow T}}{\left(1-i\Omega\tau_e^C\right)\left(1-i\Omega\tau_e^T\right)-\tau_e^C\tau_e^T/\left(\tau_t^{C\leftarrow T}\tau_t^{T\leftarrow C}\right)}$$
$$\times\frac{1}{V^C}\left(\sum_{|\vec{k}|}\frac{1}{1-i\Omega\tau_1}|M^C|^2\frac{\partial f_x^C}{\partial N}\hat{\chi}^C(\omega_s)\right)\frac{1}{V^T}\left(\sum_{|\vec{k}|}|M^T|^2\Delta f^T(\hat{\chi}^T(\omega_p)-(\hat{\chi}^T(\omega_q))^*)\right) \tag{26}$$

Finally, we give the full expressions for the scalar susceptibilities $\chi_{\rm CDM}^{C\leftarrow C}$ and $\chi_{\rm CDM}^{C\leftarrow T}$ introduced in (15) as (25) and (26) found at the top of the page. Notice how, in the limit of no interwell coupling (i.e., for $\tau_e^{T(C)}\rightarrow\tau_s$ and $1/\tau_t^{T\leftarrow C}$, $1/\tau_t^{C\leftarrow T}\rightarrow 0$), $\chi_{\rm CDM}^{C\leftarrow C}$ reduces to the expression for $\chi_{\rm CDM}$ in (16), whereas $\chi_{\rm CDM}^{C\leftarrow T}$ vanishes. These equations (with lifetimes taken to be the same for both types of wells) are used in the fit to the experimental data of Fig. 7.

APPENDIX B
PROPAGATION EFFECTS

In a realistic comparison of experimental results with theoretical predictions, it is important to keep in mind that the FWM conversion efficiency is strongly affected by propagation effects. In order to include such effects in our model, we need to solve the standard coupled-mode equations of FWM in optical amplifiers

$$\frac{dE_i^{(f)}}{dy}=T_i^{(f)}(y)E_i^{(f)}(y)\quad f:p,q$$
$$\frac{dE_i^{(s)}}{dy}=T_i^{(s)}(y)E_i^{(s)}(y)+\frac{i}{2}\frac{\omega_s\mu_0 c}{n_i}\times\sum_{j,k,l}\chi_{ijkl}S(y)E_j^{(p)}(y)E_k^{(p)}(y)\left(E_l^{(q)}(y)\right)^* \tag{27}$$

where

$$T_i^{(f)}(y)=\frac{1}{2}\left[g_i^{(f)}S(y)\left(1-i\alpha_i^{(f)}\right)-\gamma\right]+i\frac{\omega_f n_i}{c}.\quad f:p,q,s. \tag{28}$$

In these equations, y is along the direction of wave propagation, $g_i^{(f)}$ and $\alpha_i^{(f)}$ are the modal gain coefficient and linewidth enhancement factor for the i(th) component of the field at frequency ω_f, γ the internal loss coefficient and n_i the background refractive index. Finally, we defined the saturation factor $S(y)=\frac{1}{1+I(y)/I_{\rm sat}}$ where $I(y)$ and $I_{\rm sat}$ are the total optical intensity and saturation intensity of the SOA.

Solution of these equation (and use of the FWM polarization selection rules) allows us to write the FWM signal field at the SOA output ($y=L$) in terms of the input fields as follows [(9)]

$$E_i^{(s)}(L)=\left(E^{(p)}(0)\right)^2\left(E^{(q)}(0)\right)^*\cdot\left[\sum_{k=1}^{2}(p_iM_{iikk}p_kq_k^*)+M_{iiil}|_{l\neq i}p_lp_iq_l^*+M_{iili}|_{l\neq i}p_l^2q_i^*\right] \tag{29}$$

where we defined

$$M_{ijkl}=\chi_{ijkl}R_{ijkl}$$

$$R_{ijkl}=\frac{i}{2}\frac{\omega_s\mu_0 c}{n_i}\exp\left(\int_0^L dyT_i^{(s)}\right)\int_0^L dyS\times\exp\left[\int_0^y dy'\left(T_j^{(p)}+T_k^{(p)}+\left(T_l^{(q)}\right)^*-T_i^{(s)}\right)\right]. \tag{30}$$

In typical MQW SOA's, the propagation factor R_{ijkl} is also a strong function of the fields polarization, due to both the anisotropy and the wavelength-dependence of the gain coefficient and of the refractive index. These considerations are important in order to make any quantitative predictions of the dependence of the FWM signal intensity and polarization on the polarizations of the input waves.

REFERENCES

[1] M. Asada and Y. Suematsu, "Density-matrix theory of semiconductor lasers with relaxation broadening model-gain and gain suppression in semiconductor lasers," *IEEE J. Quantum Electron.*, vol. 21, pp. 434–442, 1985.

[2] G. P. Agrawal, "Gain nonlinearity in semiconductor lasers: Theory and applications to distributed feedback lasers," *IEEE J. Quantum Electron.*, vol. 23, pp. 860–868, 1987.

[3] M. P. Kesler and E. P. Ippen, "Subpicosecond gain dynamics in GaAlAs laser diodes," *Appl. Phys. Lett.*, vol. 51, pp. 1765–1767, 1987.

[4] B. N. Gomatam and A. P. DeFonzo, "Theory of hot carrier effects on nonlinear gain in GaAs-GaAlAs lasers and amplifiers," *IEEE J. Quantum Electron.*, vol. 26, pp. 1689–1704, 1990.

[5] K. L. Hall, J. Mark, E. P. Ippen, and G. Eisenstein, "Femtosecond gain dynamics in InGaAsP optical amplifiers," *Appl. Phys. Lett.*, vol. 56, pp. 1740–1742, 1990.

[6] K. L. Hall, A. M. Drawish, E. P. Ippen, U. Koren, and G. Raybon, "Femtosecond index nonlinearities in InGaAsP optical amplifiers," *Appl. Phys. Lett.*, vol. 62, pp. 1320–1322, 1993.

[7] J. Shah, *Ultrafast Spectroscopy of Semiconductors and Semiconductor Nanostructures*. Berlin, Germany: Springer-Verlag, 1996.

[8] J. E. Bowers, "High speed semiconductor laser design and performance," *Solid State Electron.*, vol. 30, no. 1, pp. 1–11, 1987.
[9] N. A. Olsson and G. P. Agrawal, "Spectral shift and distortion due to self-phase modulation of picosecond pulses in 1.5 μm optical amplifiers," *Appl. Phys. Lett.*, vol. 55, pp. 13–15, 1989.
[10] S. J. B. Yoo, "Wavelength conversion technologies for WDM network applications," *J. Lightwave Technol.* vol. 14, pp. 955–965, 1996.
[11] J. Zhou, N. Park, J. W. Dawson, K. J. Vahala, M. A. Newkirk, and B. I. Miller, "Terahertz four-wave mixing spectroscopy for study of ultrafast dynamics in a semiconductor optical amplifier," *Appl. Phys. Lett.*, vol. 63, pp. 1179–1181, 1993.
[12] W. Rideout, W. F. Sharfin, E. S. Koteles, M. O. Vassell, and B. Elman, "Well-barrier hole burning in quantum well lasers," *IEEE Photon. Technol. Lett.*, vol. 3, pp. 784–786, 1991.
[13] R. Nagarajan, T. Fukushima, S. W. Corzine, and J. E. Bowers, "Effects of carrier transport on high-speed quantum well lasers," *Appl. Phys. Lett.*, vol. 59, pp. 1835–1837, 1991.
[14] S. Weiss, J. M. Wiesenfeld, D. S. Chemla, G. Raybon, G. Sucha, M. Wegener, G. Eisenstein, C. A. Burrus, A. G. Dentai, U. Koren, B. I. Miller, H. Temkin, R. A. Logan, and T. Tanbun-Ek, "Carrier capture times in 1.5 μm multiple quantum well optical amplifiers," *Appl. Phys. Lett.*, vol. 60, pp. 9–11, 1992.
[15] S. C. Kan, D. Vassilovski, T. C. Wu, and K. Y. Lau, "On the effects of carrier diffusion and quantum capture in high speed modulation of quantum well lasers," *Appl. Phys. Lett.*, vol. 61, pp. 752–754, 1992.
[16] N. Tessler and G. Eisenstein, "On carrier injection and gain dynamics in quantum well lasers," *IEEE J. Quantum Electron.*, vol. 29, pp. 1586–1595, 1993.
[17] C. Y. Tsai, C. Y. Tsai, Y. H. Lo, R. M. Spencer, and L. F. Eastman, "Nonlinear gain coefficients in semiconductor quantum-well lasers: Effects of carrier diffusion, capture, and escape," *IEEE J. Select. Topics Quantum Electron.*, vol. 1, pp. 316–330, 1995.
[18] G. Lenz, E. P. Ippen, J. M. Wiesenfeld, M. A. Newkirk, and U. Koren, "Femtosecond dynamics of the nonlinear anisotropy in polarization insensitive semiconductor optical amplifiers," *Appl. Phys. Lett.*, vol. 68, p. 2933, 1996.
[19] G. P. Agrawal, "Population pulsations and nondegenerate four-wave mixing in semiconductor lasers and amplifiers," *J. Opt. Soc. Amer. B*, vol. 5, pp. 147–158, 1988.
[20] K. Kikuchi, M. Kakui, C. E. Zah, and T. P. Lee, "Observation of highly nondegenerate four-wave mixing in 1.5 μm traveling-wave semiconductor optical amplifiers and estimation of nonlinear gain coefficient," *IEEE J. Quantum Electron.*, vol. 28, pp. 151–156, 1992.
[21] A. Uskov, J. Mørk, and J. Mark, "Wave mixing in semiconductor laser amplifiers due to carrier heating and spectral hole burning," *IEEE J. Quantum Electron.*, vol. 30, pp. 1769–1781, 1994.
[22] A. Mecozzi, S. Scotti, A. D'Ottavi, E. Iannone, and P. Spano, "Four-wave mixing in traveling-wave semiconductor amplifiers," *IEEE J. Quantum Electron.*, vol. 31, pp. 689–699, 1993.
[23] M. C. Tatham, G. Sherlock, and L. D. Westbrook, "20 nm wavelength conversion using nondegenerate four-wave mixing," *IEEE Photon. Technol. Lett.*, vol. 5, pp. 1303–1306, 1993.
[24] J. Zhou, N. Park, J. W. Dawson, K. J. Vahala, M. A. Newkirk, and B. I. Miller, "Efficiency of broadband four-wave mixing wavelength conversion using semiconductor traveling-wave amplifiers," *IEEE Photon. Technol. Lett.*, vol. 6, pp. 50–52, 1994.
[25] R. Paiella, G. Hunziker, J. Zhou, K. J. Vahala, U. Koren, and B. I. Miller, "Polarization properties of four-wave mixing in strained semiconductor optical amplifiers," *IEEE Photon. Technol. Lett.*, vol. 8, pp. 773–775, 1996.
[26] G. Hunziker, R. Paiella, K. J. Vahala, and U. Koren, "Polarization-independent wavelength conversion at 2.5 Gb/s by dual-pump four-wave mixing in a strained semiconductor optical amplifier," *IEEE Photon. Technol. Lett.*, vol. 8, pp. 1633–1635, 1996.
[27] S. Schmitt-Rink, D. Bennhardt, V. Heuckeroth, P. Thomas, P. Haring, G. Maidorn, H. Bakker, K. Leo, D. Kim, J. Shah, and K. Kohler, "Polarization dependence of heavy-and light-hole quantum beats," *Phys. Rev. B*, vol. 46, pp. 10460–10463, 1992.
[28] W. W. Chow, S. W. Koch, and M. Sargent, III, *Semiconductor-Laser Physics*. Berlin, Germany: Springer-Verlag, 1994.
[29] M. A. Newkirk, B. I. Miller, U. Koren, M. G. Young, M. Chien, R. M. Jopson, and C. A. Burrus, "1.5 μm multiquantum-well semiconductor optical amplifier with tensile and compressively strained wells for polarization-independent gain," *IEEE Photon. Technol. Lett.*, vol. 4, pp. 406–408, 1993.
[30] G. Hunziker, R. Paiella, K. J. Vahala, and U. Koren, "Measurement of the stimulated carrier lifetime in semiconductor optical amplifiers by four-wave mixing of polarized ASE noise," *IEEE Photon. Technol. Lett.*, vpl. 9, pp. 907–909, July 1997.
[31] J. Zhou, N. Park, K. J. Vahala, M. A. Newkirk, and B. I. Miller, "Study of interwell carrier transport by terahertz four-wave mixing in an optical amplifier with tensile and compressively strained quantum wells," *Appl. Phys. Lett.*, vol. 65, pp. 1897–1899, 1994.
[32] R. Paiella, G. Hunziker, K. J. Vahala, and U. Koren, "Measurement of the interwell carrier transport lifetime in multiquantum-well optical amplifiers by polarization-resolved four-wave mixing," *Appl. Phys. Lett.*, vol. 69, pp. 4142–4144, 1996.
[33] R. Paiella and K. J. Vahala, "Four-wave mixing and generation of Tera-Hertz radiation in an alternating-strain coupled quantum-well structure," *IEEE J. Quantum Electron.*, vol. 32, pp. 721–728, 1996.

Roberto Paiella (S'97) was born in Milan, Italy, on December 11, 1970. He received the B.S. and M.S. degrees in electrical engineering from Columbia University, New York, NY, in 1993 and 1994, respectively, and is currently working toward the Ph.D. degree in applied physics at the California Institute of Technology, Pasadena, CA.

While a graduate student at Columbia, he was involved in a research project in basic surface science at the Columbia Radiation Lab. Currently, his thesis work is focused on the nonlinear optical properties of quantum-well semiconductor optical amplifiers and their application to all-optical signal processing.

Mr. Paiella is a member of Tau Beta Pi and Eta Kappa Nu.

Guido Hunziker was born on June 10 1969, in Zurich, Switzerland. He studied at the Swiss Federal Institute of Technology in Lausanne (EPFL) and at Carnegie Mellon University, Pittsburgh, PA. He received the Diplom-Physiker degree from the Swiss Federal Institute of Technology in Zurich (ETHZ) in 1993.

While working toward his degree, he joined the Opto-Electronics group at IBM Research in Zurich concentrating his research on high-power red-emitting GaInP laser diodes. In 1994, he worked with the Laser Enterprise at IBM on the beam quality of single-mode 980-nm pump laser diodes. He joined the applied physics Ph.D. program at the California Institute of Technology at the end of 1994, and his research focus is on four-wave mixing spectroscopy and wavelength conversion.

Uzi Koren, photograph and biography not available at the time of publication.

Kerry J. Vahala (S'82–M'84) received the Ph.D. degree in applied physics from the California Institute of Technology, Pasadena, CA, in 1985.

He is Professor of Applied Physics at Caltech. His research interests include semiconductor laser and fiber laser physics, high-speed dynamics in semiconductors, and semiconductor nanostructure physics and fabrication.

Dr. Vahala is a Fellow of the Optical Society of America and is currently a topical editor for IEEE PHOTONICS TECHNOLOGY LETTERS and the *Journal of Semiconductor Science and Technology*. He has also served previously as topical editor for the *Journal of the Optical Society of America*. He is the first recipient of the Richard P. Feynman Hughes Fellowship and has also received both the Presidential Young Investigator and Office of Naval Research Young Investigator Awards. In addition, he has been recognized twice by the Student Association at Caltech for excellence in teaching.